New TiO$_2$-doped Cu–Mg spinel-ferrite-based photocatalyst for degrading highly toxic rhodamine B dye in wastewater

Chinh Van Tran [a,1], Duong Duc La [a,1], Phuong Nguyen Thi Hoai [a], Ha Duc Ninh [a], Phuong Nguyen Thi Hong [b], Thu Ha T. Vu [c], Ashok Kumar Nadda [d], X. Cuong Nguyen [e,f], D. Duc Nguyen [g,h,*], Huu Hao Ngo [i,**]

[a] *Institute of Chemistry and Materials, Nghia Do, Cau Giay, Hanoi, Vietnam*
[b] *School of Chemical Engineering, Hanoi University of Science and Technology, 1 Dai Co Viet, Hanoi, Vietnam*
[c] *State Key Laboratory for Petrochemical and Refinery Technologies, Vietnamese Institute of Industrial Chemistry, Hanoi, Vietnam*
[d] *Department of Biotechnology and Bioinformatics, Jaypee University of Information Technology, Waknaghat, Solan 173234, Himachal Pradesh, India*
[e] *Laboratory of Energy and Environmental Science, Institute of Research and Development, Duy Tan University, Da Nang 550000, Vietnam*
[f] *Faculty of Environmental Chemical Engineering, Duy Tan University, Da Nang 550000, Vietnam*
[g] *Faculty of Environmental and Food Engineering, Nguyen Tat Thanh University, 300A Nguyen Tat Thanh, District 4, HCM City 755414, Vietnam*
[h] *Department of Environmental Energy Engineering, Kyonggi University, South Korea*
[i] *Centre for Technology in Water and Wastewater, School of Civil and Environmental Engineering, University of Technology Sydney, Sydney, NSW 2007, Australia*

* Corresponding author at: Faculty of Environmental and Food Engineering, Nguyen Tat Thanh University, 300A Nguyen Tat Thanh, District 4, HCM City 755414, Vietnam.
** Corresponding author.

E-mail addresses: nguyensyduc@gmail.com (D.D. Nguyen), ngohuuhao121@gmail.com (H.H. Ngo).
[1] Equal contributing authors.

ABSTRACT

The quest for finding an effective photocatalyst for environmental remediation and treatment strategies is attracting considerable attentions from scientists. In this study, a new hybrid material, Cu$_{0.5}$Mg$_{0.5}$Fe$_2$O$_4$–TiO$_2$, was designed and fabricated using coprecipitation and sol-gel approaches for degrading organic dyes in wastewater. The prepared hybrid materials were fully characterized using scanning electron microscopy, X-ray diffraction, Fourier transform infrared spectroscopy, and X-ray photoelectron spectroscopy. The results revealed that the Cu$_{0.5}$Mg$_{0.5}$Fe$_2$O$_4$–TiO$_2$ hybrid material was successfully synthesized with average particle sizes of 40.09 nm for TiO$_2$ and 27.9 nm for Cu$_{0.5}$Mg$_{0.5}$Fe$_2$O$_4$. As the calculated bandgap energy of the hybrid material was approximately 2.86 eV, it could harvest photon energy in the visible region. Results indicate that the Cu$_{0.5}$Mg$_{0.5}$Fe$_2$O$_4$–TiO$_2$ also had reasonable magnetic properties with a saturation magnetization value of 11.2 emu/g, which is a level of making easy separation from the solution by an external magnet. The resultant Cu$_{0.5}$Mg$_{0.5}$Fe$_2$O$_4$–TiO$_2$ hybrid material revealed better photocatalytic performance for rhodamine B dye (consistent removal rate in the 13.96×10^{-3} min^{-1}) compared with free-standing Cu$_{0.5}$Mg$_{0.5}$Fe$_2$O$_4$ and TiO$_2$ materials. The recyclability and photocatalytic mechanism of Cu$_{0.5}$Mg$_{0.5}$Fe$_2$O$_4$–TiO$_2$ are also well discussed.

1. Introduction

Organic dyes have been widely and effectively utilized in many industries, including, but not limited to, leather, food, mining, and paper manufacturing (Manzoor and Sharma, 2020). However, their use results in a wide dispersion of wastewater containing organic dye, which is highly hazardous, toxic, nonbiodegradable, and carcinogenic, adversely affecting human health and the environment (Robinson et al., 2001; Li et al., 2014; Sandoval et al., 2017; Kumar et al., 2019). Among the common organic dyes employed in industry, rhodamine B (RhB) is considered highly toxic and detrimental to humans and the environment, even at a small concentration of less than 1 ppm. It is widely used as a label compound in many industrial processes (Salleh et al., 2011; Merouani et al., 2010; Mostafa Hosseini Asl et al., 2018). Thus, the removal of organic dyes in general or RhB in particular from wastewater, before it discharges to receiving water bodies, is urgent and must be sustained. Many techniques, such as coagulation–flocculation, adsorption, ion exchange, degradation, photocatalysis, and combinations have

been successfully employed to treat RhB-containing wastewater (Bulut et al., 2008; Li et al., 2015; Chen et al., 2013). Of these, photo-degradation (photocatalysis) has been demonstrated to be an affordable and effective approach for RhB-containing-wastewater remediation because of its reusability, high activity, and cost-effectiveness (Bhosale and La, 2018).

A photocatalyst is a type of semiconductor material that can absorb the photon energy from sunlight to generate electron–hole pairs, which are responsible for the degradation of organic dyes (Xu et al., 2019). However, most commercial photocatalysts (such as TiO_2) have a high bandgap energy (>3.1 eV) and can only harvest photon energy in the ultraviolet region, which hinders their use in many practical applications (Zhu et al., 2019; Piña-Pérez et al., 2017). Thus, tailoring the bandgap energy, as well as functionalizing the photocatalysts, which enables them to absorb a wider range of light energy from the sunlight spectrum, have received extensive attentions from scientists worldwide in recent years (Li et al., 2011; La et al., 2020). In addition, material recyclability plays an important role in terms of feasibility and cost-effectiveness for practical wastewater treatment applications. As the majority of photocatalysts have the highest photocatalytic performance in powder form (especially at nano size), it is crucial for materials with such properties to be easily collected after each treatment cycle. One of the most common techniques for this purpose is the development of magnetic photocatalysts, which can collect the material from treated wastewater using an external magnetic field (Cho et al., 2008; Jacob et al., 2011; Dom et al., 2011; Seffati et al., 2019).

Of these magnetic materials, spinel ferrites have the highest magnetic properties (superparamagnetic), enabling them to be recovered easily by the application of external magnets (Baig and Varma, 2013; Nasir Baig et al., 2015). Spinel ferrite nanostructures typically have a chemical formula, AFe_2O_4, where Fe^{3+} is positioned at octahedral sites and A is metallic ions, such as Cu^{2+}, Mn^{2+}, Co^{2+}, Ni^{2+}, and Zn^{2+}, which are usually located in tetrahedral sites in the ferrite structure (Debnath and Das, 2020). There are three common spinel ferrite structures depending on the position of the metal ions: normal structure (A^{2+} located at the tetrahedral sites and Fe^{3+} at the octahedral sites), inverse structure (A^{2+} at octahedral sites and Fe^{3+} at both sites), and mixed structure (A^{2+} and Fe^{3+} at both sites) (Tran et al., 2020). Recently, a new trend in the proportional replacement of A^{2+} in the cubic spinel ferrite structure with other divalent metal ions has attracted increasing attention because of these interesting properties. Many metal-binary spinel ferrites have been successfully synthesized in the past few years, such as $Co_{1-2x}Ni_xMn_xFe_{2-y}Ce_yO_4$ (Almessiere et al., 2020), $CuCe_xFe_{2-x}O_4$ (Elayakumar et al., 2019), $NiFe_{2-x}V_xO_4$ ($0.0 \leq x \leq 0.3$) (Slimani et al., 2019a), $Co_{0.5}Zn_{0.5}Re_xFe_{2-x}O_4$ (Almessiere et al., 2019), and $Ca_xMg_{x-}Ni_{1-2x}Fe_2O_4$ (Slimani et al., 2019c).

Such spinel ferrites can be fabricated using many approaches, including hydrothermal, combustion, ball-milling, solid-state reaction, sol-gel, and coprecipitation methods (Roy and Bera, 2006; Asadi et al., 2020; Slimani et al., 2019b; Hannachi et al., 2015). Among these metal-binary spinel ferrites, $Cu_{0.5}Mg_{0.5}Fe_2O_4$ is a semiconducting material with remarkable magnetic properties and excellent thermal and chemical stability. It can be utilized in various sensor, adsorption, photocatalysis, and electronics applications (Zhou et al., 2015; Zaki et al., 2015). For example, $Cu_{0.5}Mg_{0.5}Fe_2O_4$ was successfully fabricated using coprecipitation methods, and the resultant spinel ferrite exhibited the highest adsorption behavior toward lead ions, with a maximum capacity of 57.7 mg/g (Tran et al., 2020).

Even with a low bandgap energy of approximately 1.7 eV and a suitable electronic structure, it is promising for effective application as a visible-active photocatalyst. However, $Cu_{0.5}Mg_{0.5}Fe_2O_4$ has only been investigated in the context of photocatalysis. It should also be noted that the combination of more than one semiconducting material to form heterogeneous photocatalysts is necessary to enable the photocatalysts to harvest photon energy in a wide range of light regions (Arifin et al., 2019).

Several spinel-ferrite–TiO_2 composites have been reported and effectively employed as photocatalysts for the degradation of organic compounds. Zhang et al. (2010) successfully fabricated a $ZnFe_2O_4/P25$ (TiO_2) nanocomposite by physically grinding $ZnFe_2O_4$ nanocubes with commercial Degussa P25 (TiO_2) at ambient temperature. The prepared $ZnFe_2O_4/TiO_2$ nanocomposite showed high photocatalytic performance toward rhodamine B with a degradation rate constant of 9.71×10^{-3} min^{-1} (Zhang et al., 2010). In another study, $(Co,Mn)Fe_2O_4$–TiO_2 composite was synthesized by a simple mixing method of commercial $(Co,Mn)Fe_2O_4$ nanoparticles with a titanium polymeric resin (a precursor of TiO_2 nanoparticles) (Neris et al., 2018). The material obtained showed reasonable photocatalytic performance toward Remazol golden yellow azo dye with a removal percentage of 90% after 16 h of UV-light irradiation. However, most of the reported spinel-based TiO_2 photocatalysts have a low dye-removal efficiency and are usually active in UV light. Thus, it is necessary to find a novel composite with high photocatalytic performance, a wide range of light harvesting, and recyclability for practical applications.

Based on an analysis of this gap in the literature, a new type of $Cu_{0.5}Mg_{0.5}Fe_2O_4$–TiO_2 hybrid material was proposed. It was fabricated using the coprecipitation method. The resultant $Cu_{0.5}Mg_{0.5}Fe_2O_4$–TiO_2 was thoroughly characterized with respect to the morphologies and the magnetic and optical properties. In this study, the photocatalytic activity of Cu–Mg spinel-ferrite-based materials toward organic dyes was investigated for the first time. A plausible photocatalytic mechanism of $Cu_{0.5}Mg_{0.5}Fe_2O_4$–TiO_2 hybrid materials for degrading organic dyes is proposed and discussed.

2. Materials and experiments

2.1. Materials

Ferric chloride hexahydrate ($FeCl_3$ $6H_2O$, 98%), copper chloride hydrate ($CuCl_2$ $2H_2O$, 99%), magnesium chloride ($MgCl_2·6H_2O$, 99%), titanium butoxide ($Ti(OBu)_4$), sodium hydroxide (NaOH, 99%), ethanol (C_2H_5OH, 99%), deionized (DI) water, and RhB dye were purchased from Sigma Aldrich. All chemicals were used as received, without further purification.
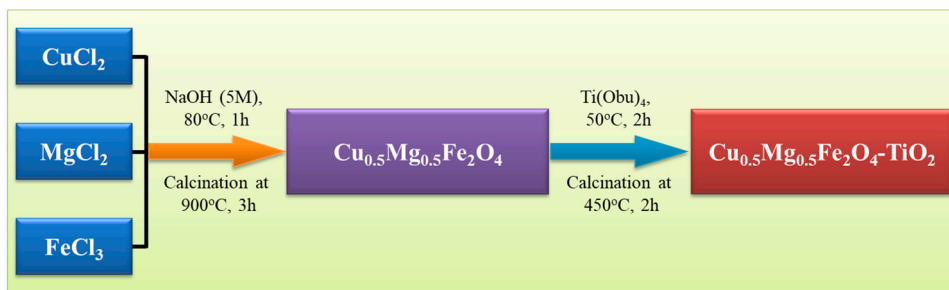
2.2. Synthesis of materials

2.2.1. $Cu_{0.5}Mg_{0.5}Fe_2O_4$ nanoparticles

The synthesis process of the $Cu_{0.5}Mg_{0.5}Fe_2O_4$ nanoparticles was adopted from previous research, i.e., chemical coprecipitation, as shown in Scheme 1 (Tran et al., 2020). The optimized molar ratio of (Cu^{2+} + Mg^{2+}:Fe^{3+}) was determined to be 1:2. In the typical procedure, 1.015 g of $CuCl_2·2H_2O$ (0.005 mol), 0.585 g of $MgCl_2$ $6H_2O$ (0.005 mol), and 5.41 g of $FeCl_3$ $6H_2O$ (0.02 mol) were gradually added to a 100-mL glass beaker containing 50 mL of DI water. The mixture was vigorously stirred using a magnetic agitator for 15 min. Then, NaOH (5 M) solution was added drop-wise to the mixture until the pH solution reached a value of 9–10. The mixture was heated to 80 °C and maintained at this temperature for 1 h with continuous stirring. The mixture was then naturally cooled to room temperature (25 °C), and then the precipitate was filtered and washed thoroughly with DI water followed by ethanol washing. The cleaned precipitate was dried at 150 °C for 8 h and then calcined at 900 °C for 3 h to obtain $Cu_{0.5}Mg_{0.5}Fe_2O_4$ spinel ferrite. The product was stored in a vacuum for further synthesis and characterization.

2.2.2. Synthesis of $Cu_{0.5}Mg_{0.5}Fe_2O_4$–TiO_2 hybrid material

The $Cu_{0.5}Mg_{0.5}Fe_2O_4$–TiO_2 hybrid material was prepared as shown in Scheme 1. Typically, 2 mL of $Ti(OBu)_4$ was dissolved in 20 mL of ethanol and then 20 mL of DI water. Subsequently, 0.5 g of $Cu_{0.5}Mg_{0.5}Fe_2O_4$ nanoparticles was gradually added to the Ti–precursor solution, heated to 50 °C, and subjected to magnetic stirring for 2 h. The

Scheme 1. Schematic diagram of the experimental setup for the synthesis of the $Cu_{0.5}Mg_{0.5}Fe_2O_4$–TiO_2 hybrid material.

precipitates were filtered, thoroughly washed, dried, and calcined at 450 °C for 2 h in air. For comparison, TiO_2 nanoparticles were fabricated under the same reaction conditions as the $Ti(OBu)_4$ precursor.

2.3. Characterization

The structure and crystallinity were analyzed by X-ray diffraction (XRD, X′Pert PRO PANalytical) with a 0.15405-nm Cu-Kα radiation source. The morphology and particle size of the samples were obtained and the elemental analysis was performed using scanning electron microscopy energy dispersive X-ray spectroscopy (SEM-EDX, Hitachi S-4600). Fourier transform infrared spectroscopy (FTIR, TENSOR II, Bruker) was used to investigate the surface functional groups of the prepared nanostructured samples. Optical absorption spectra were measured using a UV–vis spectrophotometer (Jasco V730). Magnetization measurements were performed using a vibrating sample magnetometer at room temperature. The electron–hole pair recombination rates were determined using a luminescence spectrophotometer. Liquid chromatography–mass spectrometry (LC-MS)/MS spectra were measured using a QTOF SCIEX X500R instrument (USA) with a Turbo V source and a separation column of 2.0 mm × 50 mm × 3 μm (Gemini C18 110 A$_o$, USA). The total organic carbon was determined using Multi N/C 2100s (Analytik Jena, Germany). Raman spectra were obtained using a Horiba XploRA Plus instrument (Japan).

2.4. Evaluation of photocatalytic activity

The photocatalytic performances of $Cu_{0.5}Mg_{0.5}Fe_2O_4$, TiO_2, and $Cu_{0.5}Mg_{0.5}Fe_2O_4$–TiO_2 were evaluated for the degradation of the RhB dye as a simulated pollutant under visible light using a 350-W xenon lamp, which simulated sunlight irradiation with wavelengths from UV to IR, including the visible region. The photocatalytic performance was tested using a multitube photocatalytic reactor. The distance between the light source and the reactor was 20 cm. In a typical photocatalytic test, 20 mg of the photocatalyst was added to 20 mL of a 10-ppm RhB solution. Before the photocatalytic degradation experiment commenced, the solutions were kept in the dark for 2 h to establish an absorption–desorption equilibrium. The solution was removed at certain times, and an external magnet was used to collect the photocatalysts. The photocatalytic degradation process was monitored by measuring the characteristic absorption peak at 552 nm using a UV–vis spectrophotometer.

2.5. Recyclability

The stability and reusability of the $Cu_{0.5}Mg_{0.5}Fe_2O_4$–TiO_2 photocatalyst were examined as follows: Firstly, 20 mg of photocatalyst was added to 20 mL of 10-ppm RhB and kept in the dark for 2 h before irradiation. After 3 h of light irradiation, the mixture was removed, and the photocatalyst was collected using an external magnet. The photocatalyst was washed and dried thoroughly before the next experimental cycle. The experimental procedure was repeated for five cycles to

evaluate recyclability. The removal percentage of RhB after each cycle was monitored using a UV–vis spectrophotometer.

3. Results and discussion

3.1. XRD analysis of the catalysts

The crystalline structures of the $Cu_{0.5}Mg_{0.5}Fe_2O_4$ nanoparticles, TiO_2, and $Cu_{0.5}Mg_{0.5}Fe_2O_4$–TiO_2 hybrid material hybrid nanoparticles were analyzed using XRD, as shown in Fig. 1a. The XRD pattern of $Cu_{0.5}Mg_{0.5}Fe_2O_4$ shows diffraction peaks at 2θ = 30.6°, 35.5°, 43.2°, 53.9°, 57.5°, and 62.7°, corresponding to the (220), (311), (400), (422), (511), and (440) crystal planes, respectively (Tran et al., 2020). These diffraction peaks are indexed to the cubic crystal system with the *Fd-3m* space group, which well agrees with the standard patterns of both $CuFe_2O_4$ (JCPDS 01-077-0010) and $MgFe_2O_4$ (JCPDS01-089-3084). The XRD pattern of TiO_2 displayed diffraction peaks at 2θ = 25.8°, 38.2°, 48.4°, 53.5°, 54.8°, 63.1°, 68.8°, and 70.7°, which were assigned to the (101), (112), (200), (105), (211), (204), (116), and (220) planes of the anatase phase (JCPDS 01-071-1167). The characteristic diffraction peaks of $Cu_{0.5}Mg_{0.5}Fe_2O_4$ (S) and TiO_2 (A) also appeared in the XRD pattern of the $Cu_{0.5}Mg_{0.5}Fe_2O_4$–TiO_2 hybrid material, indicating the successful fabrication of the $Cu_{0.5}Mg_{0.5}Fe_2O_4$–TiO_2 hybrid material. Fig. 1b shows the EDX spectra of $Cu_{0.5}Mg_{0.5}Fe_2O_4$ and $Cu_{0.5}Mg_{0.5}Fe_2O_4$–TiO_2. This also indicates that all elements of Cu, Mg, Fe, Ti, and O appear in the EDX spectra of the nanoparticles. Furthermore, the percentages of these elements are consistent with the stoichiometry ratios of $Cu_{0.5}Mg_{0.5}Fe_2O_4$ and $Cu_{0.5}Mg_{0.5}Fe_2O_4$–TiO_2.

3.2. SEM studies

The morphologies of the $Cu_{0.5}Mg_{0.5}Fe_2O_4$, TiO_2, and $Cu_{0.5}Mg_{0.5}Fe_2O_4$–TiO_2 hybrid materials were observed by SEM and transmission electron microscopy (TEM) (Fig. 2). Fig. 2a and b shows that, while TiO_2 has a spherical shape with a diameter in the 10–20-nm range, $Cu_{0.5}Mg_{0.5}Fe_2O_4$ has a cube-like shape with an average particle size of approximately 30 nm. The SEM and TEM images of the $Cu_{0.5}Mg_{0.5}Fe_2O_4$–TiO_2 (Fig. 2c and d, respectively) reveal the hybrid morphologies of both TiO_2 and $Cu_{0.5}Mg_{0.5}Fe_2O_4$. These particles tend to aggregate, which might result from the high static affinities of the surfaces of the TiO_2 and $Cu_{0.5}Mg_{0.5}Fe_2O_4$ particles. The particle size distributions of the TiO_2, $Cu_{0.5}Mg_{0.5}Fe_2O_4$, and $Cu_{0.5}Mg_{0.5}Fe_2O_4$–TiO_2 hybrid materials were initially determined by ImageJ software. As obtained from the SEM images, they were 17.76, 27.45, and 96.69 nm, respectively (Supplementary material, Fig. S1). To determine the average particle size of the TiO_2, $Cu_{0.5}Mg_{0.5}Fe_2O_4$, and $Cu_{0.5}Mg_{0.5}Fe_2O_4$–TiO_2 from the XRD patterns, the Debye–Scherrer formula (D = k λ/(B cos θ), where k, λ, B, and θ are the Scherrer constant (0.89), X-ray wavelength (0.1504 nm), width of the peak at half maximum intensity (radian), and angle of diffraction, respectively, were employed. The results show that the average diameters of the $Cu_{0.5}Mg_{0.5}Fe_2O_4$ and TiO_2 nanoparticles were 29.5 and 16.4 nm, respectively. These sizes agree well with the SEM observations.

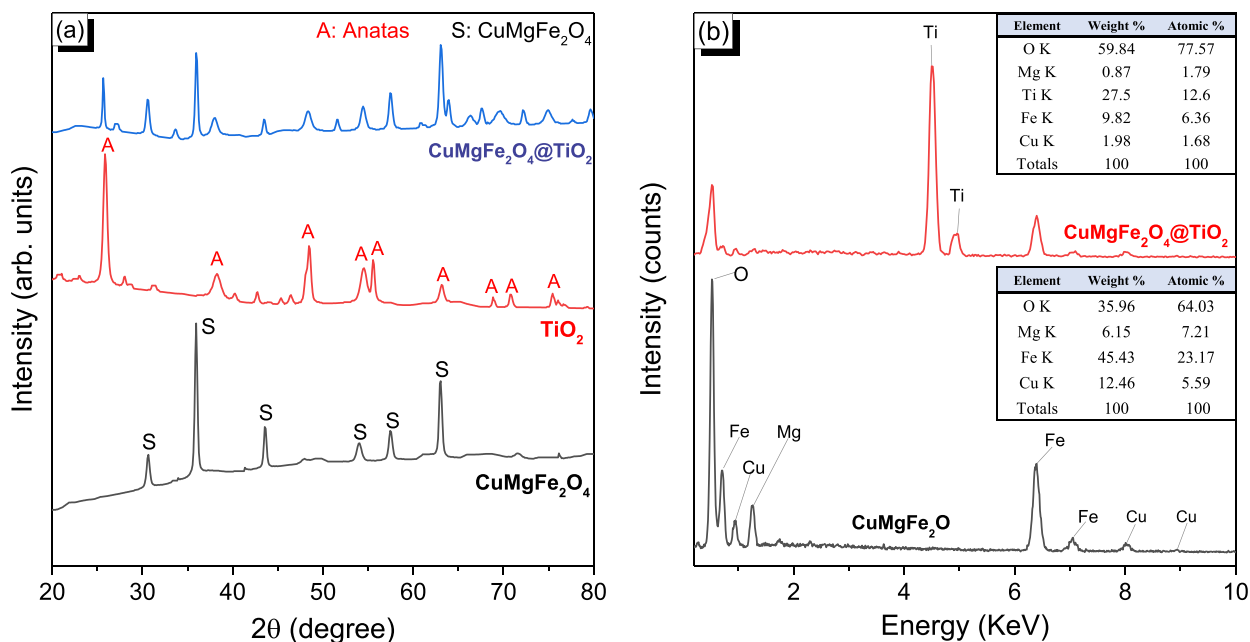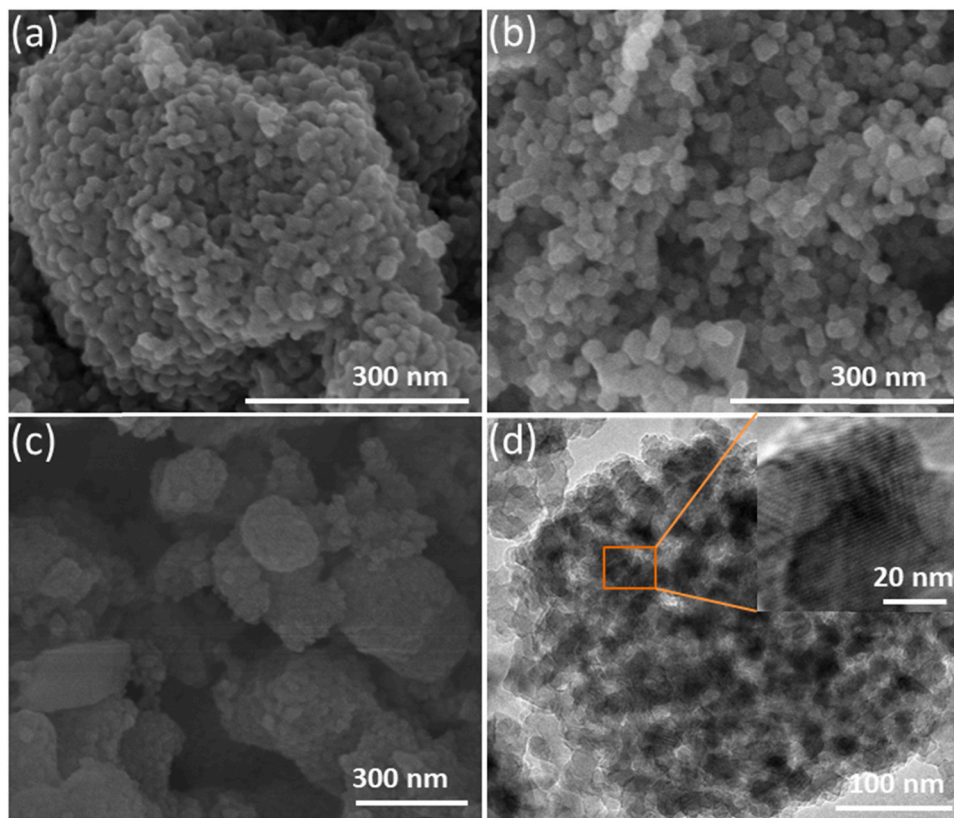**Fig. 1.** XRD pattern (a) and EDX analysis (b) of the samples.

Fig. 2. SEM images of (a) TiO$_2$, (b) Cu$_{0.5}$Mg$_{0.5}$Fe$_2$O$_4$, and (c, d) Cu$_{0.5}$Mg$_{0.5}$Fe$_2$O$_4$–TiO$_2$ hybrid material.

Moreover, in the Cu$_{0.5}$Mg$_{0.5}$Fe$_2$O$_4$–TiO$_2$ hybrid material, while the average diameter determined by the Debye–Scherrer formula of Cu$_{0.5}$Mg$_{0.5}$Fe$_2$O$_4$ (27.9 nm) is similar to that of the free-standing Cu$_{0.5}$Mg$_{0.5}$Fe$_2$O$_4$ (29.5 nm), the average size of the TiO$_2$ in the hybrid material significantly increased to 40.09 nm compared with 16.4 nm for the free-standing TiO$_2$. This could be caused by the presence of Cu$_{0.5}$Mg$_{0.5}$Fe$_2$O$_4$ as nucleation and growth sites for the larger TiO$_2$

crystals.

3.3. FT-IR, Raman, and magnetization analysis of the catalysts

The chemical natures of TiO$_2$, Cu$_{0.5}$Mg$_{0.5}$Fe$_2$O$_4$, and Cu$_{0.5}$Mg$_{0.5}$Fe$_2$O$_4$–TiO$_2$ were studied using FTIR spectroscopy, as shown in Fig. 3a. The absorption peaks around 3400 and 1600 cm^{-1} were observed in the
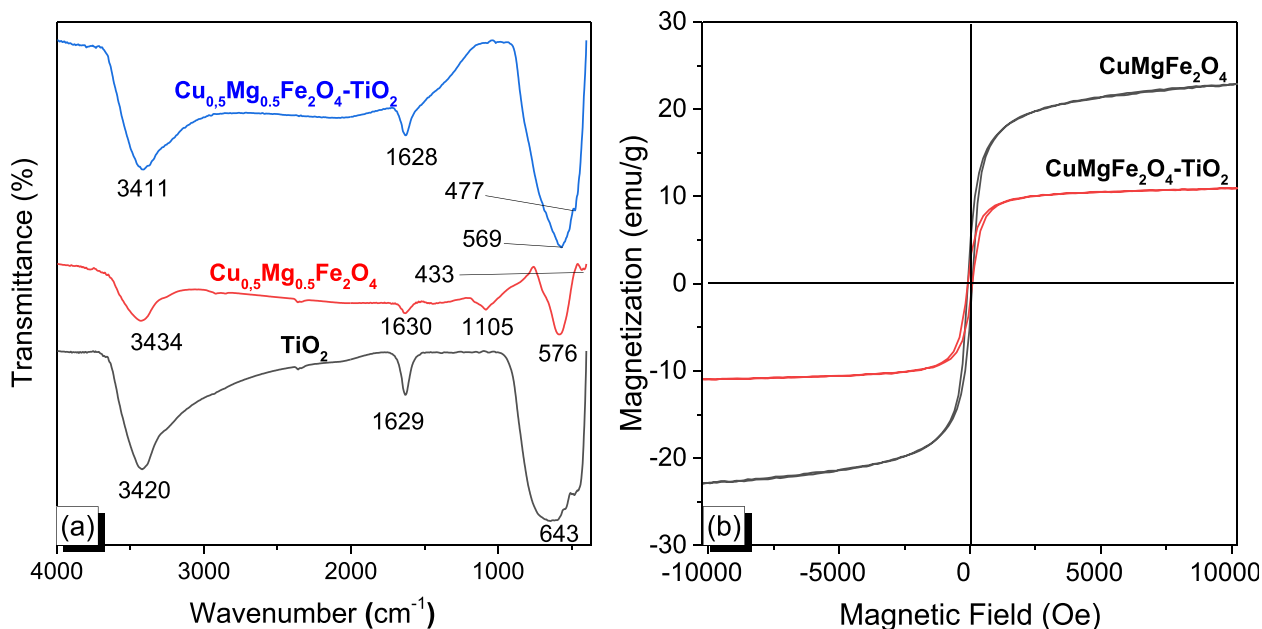
Fig. 3. (a) FTIR spectra of TiO_2, $Cu_{0.5}Mg_{0.5}Fe_2O_4$, and $Cu_{0.5}Mg_{0.5}Fe_2O_4$–TiO_2 and (b) magnetic hysteresis loops of $Cu_{0.5}Mg_{0.5}Fe_2O_4$ nanoparticles and $Cu_{0.5}Mg_{0.5}Fe_2O_4$–TiO_2 hybrid material.

FTIR spectra of TiO_2, $Cu_{0.5}Mg_{0.5}Fe_2O_4$, and $Cu_{0.5}Mg_{0.5}Fe_2O_4$–TiO_2, and they are assigned to the sketching vibration of the O–H group from adsorbed water or humidity on the surface of the materials. In the spinel ferrite structure, the metal ions are situated in two different sublattices, designated as tetrahedral (A-site) and octahedral (B-site) (Mohit et al., 2014). In the FTIR spectrum of $Cu_{0.5}Mg_{0.5}Fe_2O_4$, the higher absorption bands were absorbed at 576 and 433 cm^{-1}, corresponding to the intrinsic stretching vibrations of the metal–oxygen bond at the tetrahedral site M_{tetra}–O and the octahedral site M_{octa}–O. This confirms the formation of the spinel structure, and the results are consistent with those reported by Ahmed et al. (2012). The FTIR spectrum of TiO_2 shows a broad band at 643 cm^{-1}, which is attributed to the Ti–O–Ti stretching mode. The absorption bands of TiO_2 and $Cu_{0.5}Mg_{0.5}Fe_2O_4$ in the range of 385–650 cm^{-1} were also observed in the FTIR spectrum of $Cu_{0.5}Mg_{0.5}Fe_2O_4$–TiO_2. This demonstrates the successful formation of the $Cu_{0.5}Mg_{0.5}Fe_2O_4$–TiO_2 hybrid material (Hafeez et al., 2018).

The phase compositions of the TiO_2, $Cu_{0.5}Mg_{0.5}Fe_2O_4$, and $Cu_{0.5}Mg_{0.5}Fe_2O_4$–TiO_2 hybrid materials were further investigated using Raman spectroscopy (Supplementary material, Fig. S2). The characteristic peaks appearing at 196, 336, 484, 538, and 698 cm^{-1} in the Raman spectrum of the $Cu_{0.5}Mg_{0.5}Fe_2O_4$ samples were assigned to the vibration modes of T_{1g}, E_{2g}, T_{2g}, F_{2g}, and A_{1g}, respectively, of the typical spinel ferrite (Hafeez et al., 2018). In the Raman spectrum of TiO_2, the typical E_g vibration mode appeared at 142.9, 195.1, and 395 cm^{-1}, an A_{1g} or B_{1g} mode appeared at 512.5 cm^{-1}, and the peak at 638 cm^{-1} is assigned to the A_{1g} vibration mode, confirming that the TiO_2 nanoparticles are in an anatase form (Golshan et al., 2018). All the observed peaks in the Raman spectrum of the hybrid material are assigned to the anatase TiO_2, which could result from the coverage of TiO_2 nanoparticles on the surface of the $Cu_{0.5}Mg_{0.5}Fe_2O_4$ particles.

The magnetic properties of the prepared materials were investigated using hysteresis loops, which show the variation in magnetization (M, emu/g) and magnetic field (H, Oe) (Fig. 3b). The saturation magnetizations of $Cu_{0.5}Mg_{0.5}Fe_2O_4$ and $Cu_{0.5}Mg_{0.5}Fe_2O_4$–TiO_2 are based on what is shown in the figure: 23.1 and 11.2 emu/g, respectively. The lower saturation magnetization value of $Cu_{0.5}Mg_{0.5}Fe_2O_4$–TiO_2 compared with that of $Cu_{0.5}Mg_{0.5}Fe_2O_4$ results from the presence of nonmagnetic TiO_2 in the hybrid materials. The coercivity (H_c) of both $Cu_{0.5}Mg_{0.5}Fe_2O_4$ and $Cu_{0.5}Mg_{0.5}Fe_2O_4$–TiO_2 remained at 83 Oe.

However, with a saturation magnetization value of 11.2 emu/g, $Cu_{0.5}Mg_{0.5}Fe_2O_4$–TiO_2 is easily separated from the solution using an external magnet. This is one of the key properties that makes possible the practical application of the materials (Golshan et al., 2018). The nitrogen adsorption isotherm and pore size distribution (inset) of the $Cu_{0.5}Mg_{0.5}Fe_2O_4$–TiO_2 hybrid materials are shown in Supplementary material, Fig. S3. The results reveals that the Brunauer–Emmett–Teller surface area, pore volume, and average pore width of the $Cu_{0.5}Mg_{0.5}Fe_2O_4$–TiO_2 were found to be 27.08 m^2/g, 0.072 cm^3/g, and 10.11 nm, respectively.

3.4. XPS analysis

The chemical and electronic compositions of the $Cu_{0.5}Mg_{0.5}Fe_2O_4$–TiO_2 hybrid material were analyzed by XPS, and the results are shown in Fig. 4. The surface XPS profile (Fig. 4a) reveals the presence of Fe, Cu, Mg, Ti, and O in the stoichiometry ratio of $Cu_{0.5}Mg_{0.5}Fe_2O_4$–TiO_2. Two characteristic peaks are observed at binding energies of 723.88 and 710.28 eV, corresponding to Fe $2p_{1/2}$ and Fe $2p_{3/2}$, respectively, from Fe^{3+} at the octahedral site (Fig. 4b) (Ren et al., 2017; Nakhate and Yadav, 2017; Qin et al., 2018). The peak at 1302.38 eV is related to Mg 1s (Fig. 4c), which reveals the oxidation state of Mg^{2+} in $Cu_{0.5}Mg_{0.c5}Fe_2O_4$–TiO_2 (Kang et al., 2015; Shen et al., 2013). The characteristic peaks at 952.28 and 932.68 eV for the Cu $2p_{1/2}$ and Cu $2p_{3/2}$, respectively, are assigned to Cu^{2+} on the octahedral site (Fig. 4d) (Reitz et al., 2012). The core-level XPS profile of the Ti 2p reveals two characteristic peaks at 464.08 and 458.28 eV, which are related to Ti $2p_{1/2}$ and Ti $2p_{3/2}$, respectively, from the Ti^{4+} oxidation state in pristine TiO_2. The peak located at 529.58 eV with a broad shoulder related to O 1s can be attributed to the reduction state of oxygen in the lattice of $Cu_{0.5}Mg_{0.5}Fe_2O_4$ and in TiO_2.

3.5. Optical properties

Fig. 5a shows the diffuse reflectance UV–vis spectra of the TiO_2, $Cu_{0.5}Mg_{0.5}Fe_2O_4$, and $Cu_{0.5}Mg_{0.5}Fe_2O_4$–TiO_2 hybrid materials. The figure shows that, while TiO_2 is only absorbed strongly in the UV region (<420 nm), $Cu_{0.5}Mg_{0.5}Fe_2O_4$ has a wide range of absorption from the UV to the visible region (200–850 nm). The $Cu_{0.5}Mg_{0.5}Fe_2O_4$–TiO_2
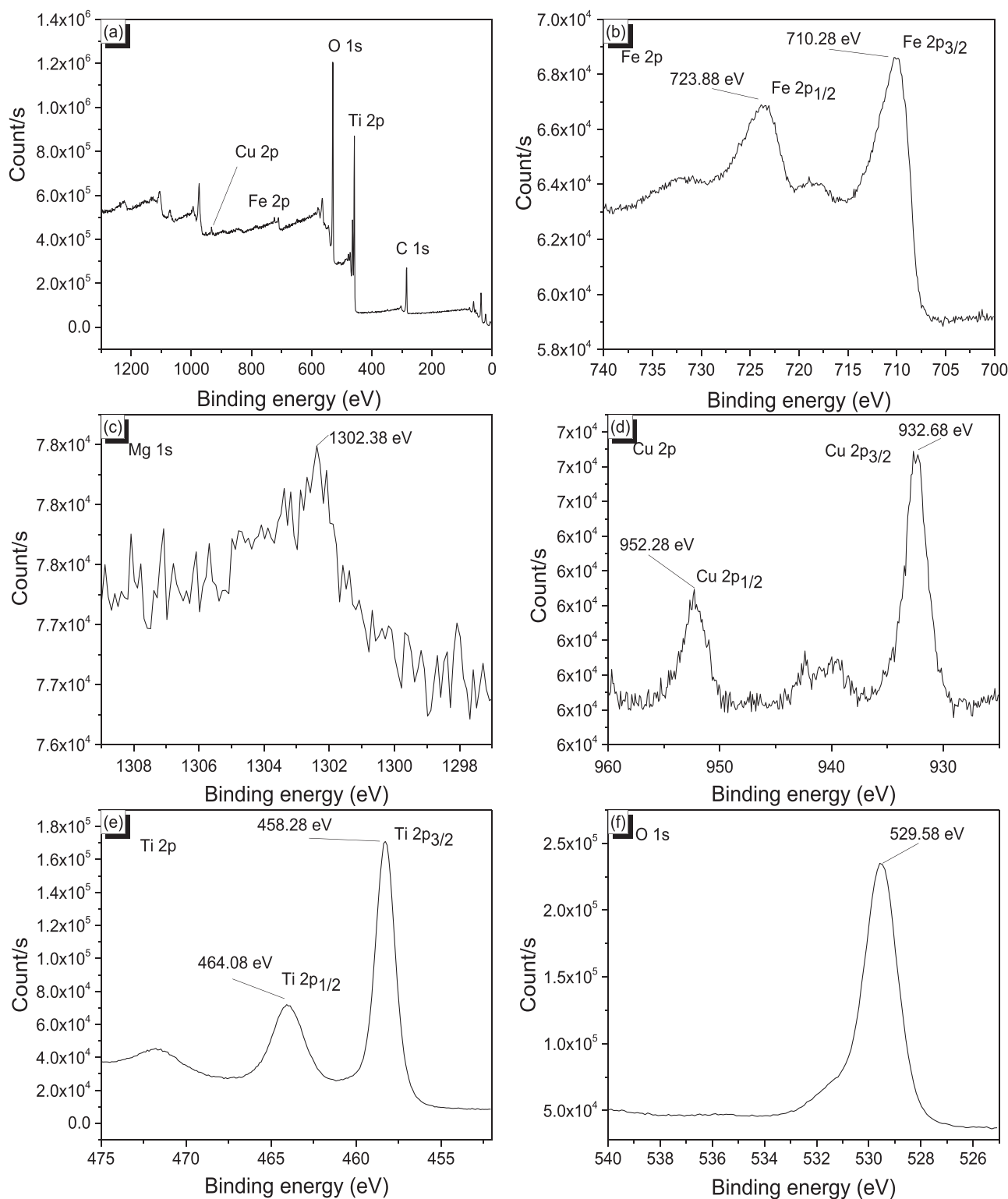
Fig. 4. (a) XPS survey spectrum of the $Cu_{0.5}Mg_{0.5}Fe_2O_4$–TiO_2 hybrid material and the core-level XPS profiles of (b) Fe 2p, (c) Mg 1s, (d) Cu 2p, (e) Ti 2p, and (f) O 1s.

hybrid material, a combination of free-standing TiO_2 and $Cu_{0.5}Mg_{0.5}$-Fe_2O_4, absorbed more light energy in both near-UV light and visible light. This wider absorption wavelength range of the hybrid material greatly favors photocatalytic applications. The optical absorption strength depends on the difference between the photon energy and bandgap, as shown in the following equation:

$$(\alpha h\upsilon)^{1/n} = A(h\upsilon - E_g) \tag{1}$$

Here, h is Planck's constant (6626.10^{-34} Js), υ is the light speed (3.10^8 ms^{-1}), α is the absorption coefficient, E_g is the bandgap energy, and A is the absorption intensity. Based on this equation, $(\alpha h\upsilon)^2$ versus $h\upsilon$ was plotted to determine the bandgap energy (Tauc method), and the results are shown in Fig. 5b. From the Tauc plot, the bandgap energies of $Cu_{0.5}Mg_{0.5}Fe_2O_4$, $Cu_{0.5}Mg_{0.5}Fe_2O_4$–TiO_2, and TiO_2 were calculated to be 1.65, 2.86, and 3.25 eV, respectively. This indicates that the successful

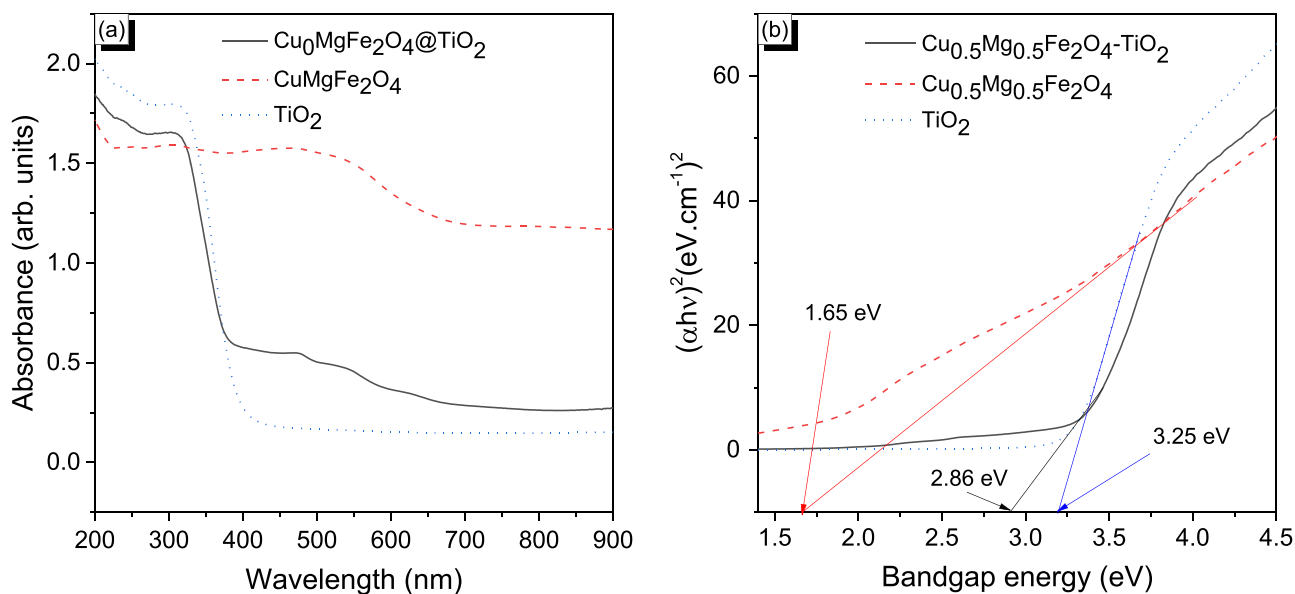**Fig. 5.** (a) UV–vis absorption spectra and (b) Tauc plot of the TiO_2, $Cu_{0.5}Mg_{0.5}Fe_2O_4$, and $Cu_{0.5}Mg_{0.5}Fe_2O_4$–TiO_2 hybrid materials.

incorporation of $Cu_{0.5}Mg_{0.5}Fe_2O_4$ and TiO_2 makes possible a new semiconductor with a bandgap energy in the visible region.

3.6. Photoluminescence study

For an effective photocatalyst, charge recombination must be minimized because electrons and holes directly participate in photocatalytic reduction. The recombination of photo-induced electrons and holes releases energy in the form of photoluminescence (PL). Hence, PL spectrum analysis is a powerful technique for studying the charge recombination of semiconductors. The PL spectra of TiO_2, $Cu_{0.5}Mg_{0.5}Fe_2O_4$, and $Cu_{0.5}Mg_{0.5}Fe_2O_4$–TiO_2 are shown in Fig. 6. A broad peak at around 500–550 nm was observed for TiO_2, $Cu_{0.5}Mg_{0.5}Fe_2O_4$, and $Cu_{0.5}Mg_{0.5}Fe_2O_4$–TiO_2. The PL spectrum of $Cu_{0.5}Mg_{0.5}Fe_2O_4$–TiO_2 highlights a lower PL intensity than that of TiO_2 and $Cu_{0.5}Mg_{0.5}Fe_2O_4$. This indicates that, after TiO_2 was leaded on $Cu_{0.5}Mg_{0.5}Fe_2O_4$, the recombination of photo-induced electron–hole pairs was significantly reduced (Arifin et al., 2019).

4. Photocatalytic study

The photocatalytic activities of the as-prepared samples were investigated through the degradation of RhB under simulated sunlight irradiation. Prior to light irradiation, a certain amount of photocatalyst
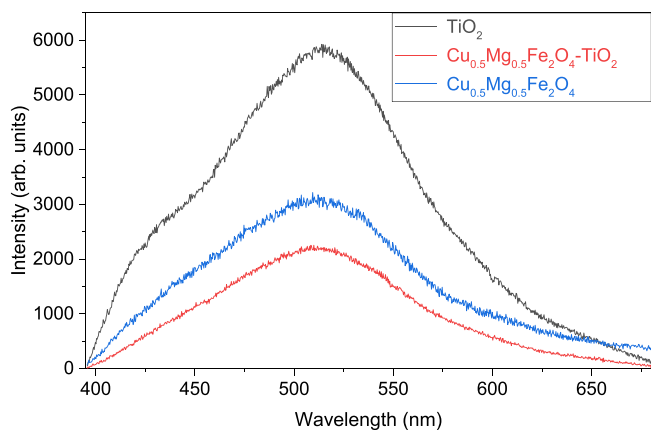

Fig. 6. PL spectra of TiO_2 and $Cu_{0.5}Mg_{0.5}Fe_2O_4$–TiO_2.

was introduced into the RhB solution and stirred in the dark for 2 h to establish an absorption–desorption equilibrium. The absorption behavior of TiO_2 and $Cu_{0.5}Mg_{0.5}Fe_2O_4$–TiO_2 was negligible. Fig. 7a and b shows the change in RhB concentration upon light irradiation with and without the presence of the $Cu_{0.5}Mg_{0.5}Fe_2O_4$–TiO_2 photocatalyst. It is clear that, in the presence of the photocatalyst, the RhB concentration significantly decreased. After 180 min, most of the RhB was degraded. Fig. 7c shows the photocatalytic performance of TiO_2, $Cu_{0.5}Mg_{0.5}Fe_2O_4$, and $Cu_{0.5}Mg_{0.5}Fe_2O_4$–TiO_2 toward the RhB dyes. In the absence of the photocatalyst, almost no RhB was degraded. However, when the photocatalysts were present, the RhB degraded significantly. It is evident that the photocatalytic performance of TiO_2 was better than that of $Cu_{0.5}Mg_{0.5}Fe_2O_4$ but worse than that of the $Cu_{0.5}Mg_{0.5}Fe_2O_4$–TiO_2 hybrid material. While the RhB removal efficiencies of TiO_2 and $Cu_{0.5}Mg_{0.5}Fe_2O_4$ were 52.7% and 21.5%, respectively, the removal efficiency of $Cu_{0.5}Mg_{0.5}Fe_2O_4$–TiO_2 was almost 100% after 180 min of simulated sunlight irradiation. This strongly suggests that the TiO_2 and $Cu_{0.5}Mg_{0.5}Fe_2O_4$ composite significantly improves the photocatalytic performance.

The kinetics of the photocatalytic reaction were determined using a pseudo-first-order kinetics model $Ln(C/C_o) = -kt$, where C_o is the initial concentration of the RhB solution (mg/L), C is the concentration of MB at time t (mg/L), and slope k is the apparent reaction rate constant (min^{-1}). The results are presented in Fig. 7d. The values of the photodegradation rate constant (k) of TiO_2, $Cu_{0.5}Mg_{0.5}Fe_2O_4$, and $Cu_{0.5}Mg_{0.5}Fe_2O_4$–TiO_2 were 3.24×10^{-3}, 1.06×10^{-3}, and 13.96×10^{-3} min^{-1}, respectively (Table 1). The rate constants of $Cu_{0.5}Mg_{0.5}Fe_2O_4$–TiO_2 are 4.3 and 13.1 times higher than those of the free-standing TiO_2 and $Cu_{0.5}Mg_{0.5}Fe_2O_4$, respectively. These results demonstrate that the $Cu_{0.5}Mg_{0.5}Fe_2O_4$-TiO_2 hybrid materials remarkably improved the photocatalytic activity of both TiO_2 and $Cu_{0.5}Mg_{0.5}Fe_2O_4$.

The similar spinel-ferrite-based TiO_2 photocatalytic performances toward organic dyes are listed in Table 2. Compared with similar materials, the $Cu_{0.5}Mg_{0.5}Fe_2O_4$–TiO_2 hybrid material shows superior photocatalytic performance for the photodegradation of RhB under simulated sunlight irradiation.

The stability and reusability of the $Cu_{0.5}Mg_{0.5}Fe_2O_4$–TiO_2 photocatalyst were studied for five cycles of RhB degradation under simulated sunlight irradiation, as shown in Fig. 8. The photocatalyst was recovered using an external magnetic field after each cycle of the photocatalytic reaction. The figure clearly shows that the removal efficiency of RhB
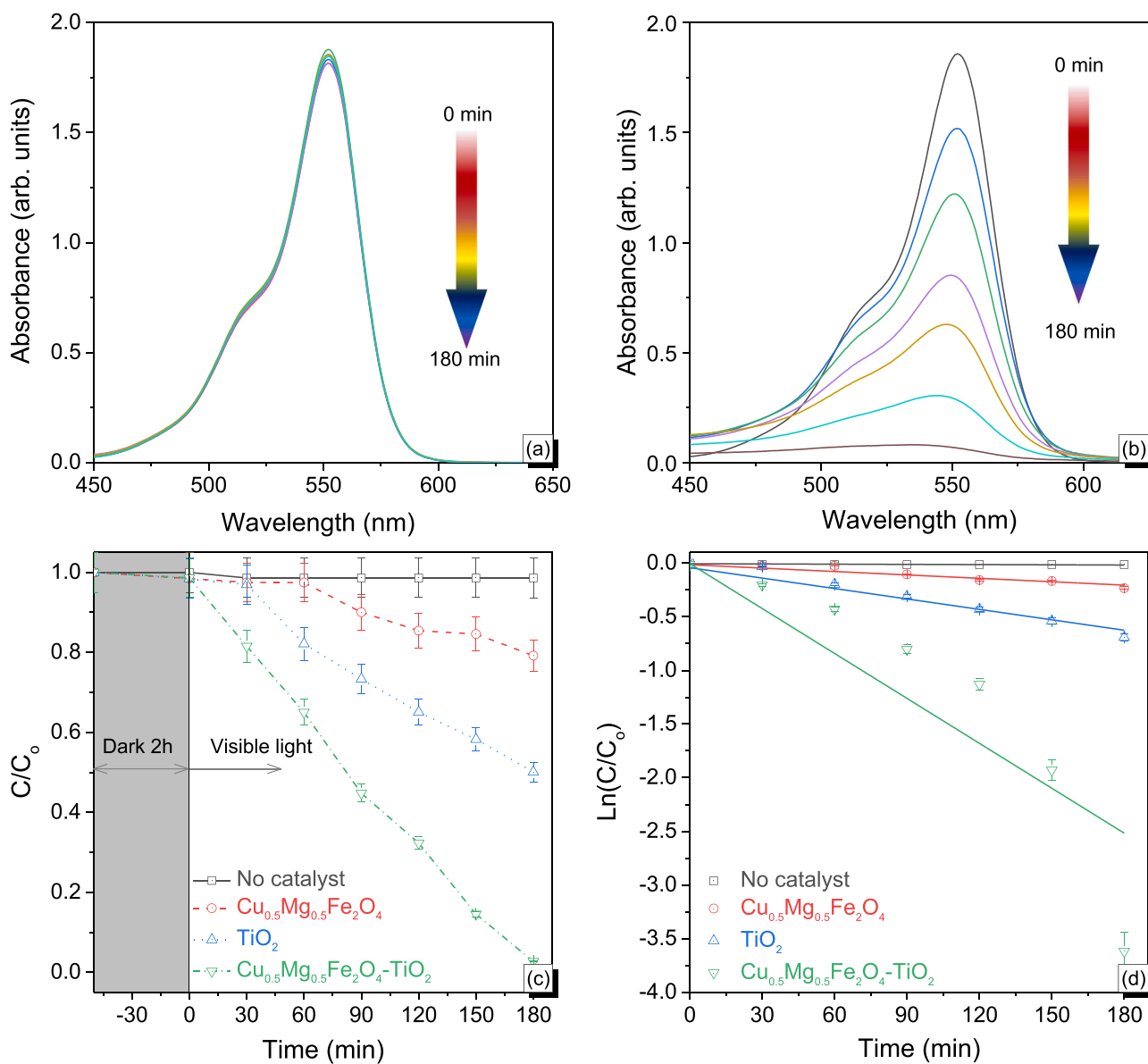
Fig. 7. Effect of treatment time on the RhB removal performance with (a) no photocatalyst and (b) $Cu_{0.5}Mg_{0.5}Fe_2O_4$–TiO_2 photocatalyst, and (c) photocatalytic performance and (d) kinetics simulation curve of the as-prepared samples for RhB degradation under simulated irradiation conditions.

Table 1
Apparent reaction rate constant (k) and photodegradation efficiency of the samples for RhB initial concentration of 10 ppm.

Catalysts	k (10^{-3} min^{-1})	Photodegradation efficiency (%)
TiO_2	3.24	52.7
$Cu_{0.5}Mg_{0.5}Fe_2O_4$	1.06	21.5
$Cu_{0.5}Mg_{0.5}Fe_2O_4$–TiO_2	13.96	98.4

when using the $Cu_{0.5}Mg_{0.5}Fe_2O_4$–TiO_2 photocatalyst declined minimally after five cycles of photocatalytic reaction with a reduction of only 6.8%. This indicates that the synthesized $Cu_{0.5}Mg_{0.5}Fe_2O_4$–TiO_2 hybrid material has high photocatalytic activity and retains good stability and reusability, which is very promising for treating wastewater containing dyes.

The intermediates during the photodegradation of RhB over the $Cu_{0.5}Mg_{0.5}Fe_2O_4$–TiO_2 photocatalyst were monitored by LC–MS/MS, as shown in Supplementary material, Fig. S4. The m/z peak values at approximately 443, 415, 399, 387, 371, and 343 (M$^+$) were assigned to

RhB, *N,N*-diethyl-*N*-ethylrhodamine, *N,N*-diethyl-rhodamine, *N*-ethyl-*N*-ethylrhodamine, *N*-ethylrhodamine, and rhodamine, respectively, in which RhB is a precursor and the other five compounds are intermediates (Liu et al., 2017). After N-deethylation, the C—N bonds are cleaved into small molecules of phenol and benzoic acid (Du et al., 2016). These small aromatic molecules further experience a ring-opening process before mineralizing to form CO_2 and H_2O environmentally friendly products (Natarajan et al., 2013). The mineralization of small aromatic compounds to form CO_2 and H_2O was confirmed by total organic carbon analysis (Supplementary material, Fig. S5).

To investigate the role of free radicals (O*$-_2$, *OH, and h$^+$) generated during the photodegradation of RhB by the $Cu_{0.5}Mg_{0.5}Fe_2O_4$–TiO_2 photocatalyst, trapping experiments were carried out with 1,4-benzoquinone (BQ) for O_2^{*-} scavenging, isopropyl alcohol (IPA) for *OH scavenging, and ammonium oxalate (AO) for h$^+$ scavenging (Jadhav et al., 2020) (Fig. 9). The presence of the radical-trapping agent significantly reduced the degradation percentage of RhB. The removal percentages of RhB by the $Cu_{0.5}Mg_{0.5}Fe_2O_4$–TiO_2 photocatalyst were
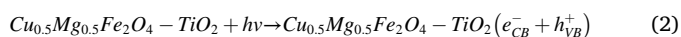
Table 2

Comparison of photocatalytic performance of several spinel-ferrite-based TiO_2 composites for organic dye degradation.

Catalyst	Light sources	Dyes	Degradation rate constant	Refs.
$ZnFe_2O_4$–TiO_2	UV–vis region	Rhodamine B	9.71×10^{-3}	(Zhang et al., 2010)
$(Co,Mn)Fe_2O_4$–TiO_2	UV–vis region	Remazol golden yellow azo dye	90%, 16 h	(Neris et al., 2018)
$CuFe_2O_4/TiO_2$	Visible	Methylene blue	11.3×10^{-3}	(Arifin et al., 2019)
$TiO_2/NiFe_2O_4$	Visible	Methyl orange	1.7×10^{-3}	(Šutka et al., 2016)
$Co_{0.5}Zn_{0.25}Ni_{0.25}Fe_2O_4$–$TiO_2$	Solar	Methyl orange	95%, 6 h	(Ciocarlan et al., 2018)
$Co_{0.5}Zn_{0.25}Cu_{0.25}Fe_2O_4$–$TiO_2$	Solar	Methyl orange	50%, 6 h	(Ciocarlan et al., 2018)
$Co_{0.5}Zn_{0.25}Mg_{0.25}Fe_2O_4$–$TiO_2$	Solar	Methyl orange	71%, 6 h	(Ciocarlan et al., 2018)
$Co_{0.5}Zn_{0.25}Mn_{0.25}Fe_2O_4$–$TiO_2$	Solar	Methyl orange	72%, 6 h	(Ciocarlan et al., 2018)
$Cu_{0.5}Mg_{0.5}Fe_2O_4$–TiO_2	Simulated sunlight	Rhodamine B	13.96×10^{-3} (98.4%, 3 h)	This work
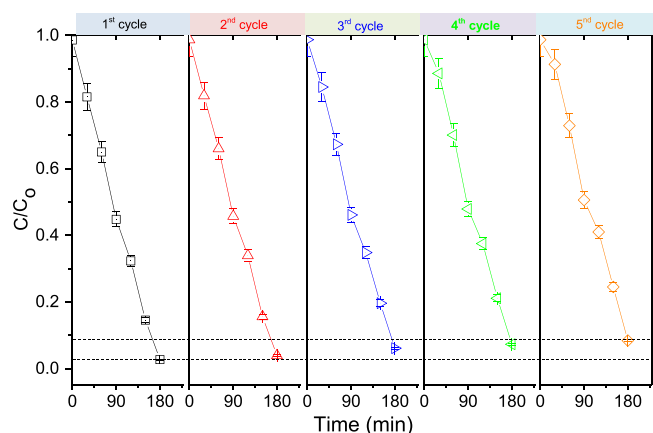
Fig. 8. Recyclability of $Cu_{0.5}Mg_{0.5}Fe_2O_4$–TiO_2 photocatalyst for RhB degradation.
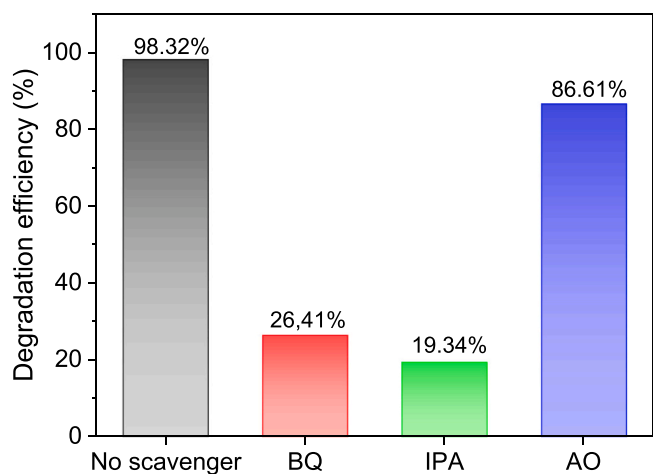
Fig. 9. Photodegradation of RhB by hybrid materials in the presence of various radical trapping agents: 1,4-benzoquinone (BQ), isopropyl alcohol (IPA), and ammonium oxalate (AO).

26.41%, 19.34%, and 86.61% in the presence of BQ, IPA, and AO, respectively. This indicates that *OH is the main active species participating in the photodegradation of RhB dye by the $Cu_{0.5}Mg_{0.5}Fe_2O_4$–TiO_2 photocatalyst.

Based on the above results and discussion, the possible mechanisms of the photodegradation activity of the $Cu_{0.5}Mg_{0.5}Fe_2O_4$–TiO_2 hybrid material can be proposed as follows (Fig. 10):

$$Cu_{0.5}Mg_{0.5}Fe_2O_4 - TiO_2 + hv \rightarrow Cu_{0.5}Mg_{0.5}Fe_2O_4 - TiO_2\left(e_{CB}^- + h_{VB}^+\right) \tag{2}$$

$$e_{CB}^- + O_2 \rightarrow O_2^{-*} \tag{3}$$

$$O_2^{-*} + H_2O \rightarrow OH^* + OOH^- \tag{4}$$

$$h_{VB}^+ + H_2O \rightarrow OH^* + H^+ \tag{5}$$

$$OH^* + RhB \rightarrow CO_2 + H_2O \tag{6}$$

When the $Cu_{0.5}Mg_{0.5}Fe_2O_4$–TiO_2 hybrid material was irradiated under simulated sunlight, electron–hole pairs were generated from the $Cu_{0.5}Mg_{0.5}Fe_2O_4$ and TiO_2 semiconductors. The photogenerated electrons were transferred from the conductive band of $Cu_{0.5}Mg_{0.5}Fe_2O_4$ to the conductive band of TiO_2 through the interface and reduced O_2 in water to O_2^{-*}. Conversely, the photogenerated holes in TiO_2 were transferred to the valence band of $Cu_{0.5}Mg_{0.5}Fe_2O_4$ and participated in the redox reactions by forming OH* radicals and oxidizing RhB to CO_2 and H_2O.

5. Conclusions

A $Cu_{0.5}Mg_{0.5}Fe_2O_4$–TiO_2 hybrid material was successfully fabricated using coprecipitation and sol-gel approaches. The prepared $Cu_{0.5}Mg_{0.5}Fe_2O_4$–TiO_2 hybrid material shows good integration of the TiO_2 and $Cu_{0.5}Mg_{0.5}Fe_2O_4$ nanoparticles with a bandgap energy of approximately 2.86 eV, which enabled the material to harvest the photon energy in the visible regions for photocatalytic application. Furthermore, combining the $Cu_{0.5}Mg_{0.5}Fe_2O_4$ and TiO_2 semiconductors significantly increased the charge separation, which in turn enhanced the photocatalytic performance. This was evident from the superior photocatalytic performance of the $Cu_{0.5}Mg_{0.5}Fe_2O_4$–TiO_2 hybrid material compared with that of free-standing $Cu_{0.5}Mg_{0.5}Fe_2O_4$ and TiO_2 materials with an RhB degradation rate constant of as much as 13.96×10^{-3} min^{-1}. The $Cu_{0.5}Mg_{0.5}Fe_2O_4$–TiO_2 also exhibited high recyclability with a removal efficiency of only 6.8% after five cycles of photocatalytic reaction to RhB dye. With high photocatalytic performance, recyclability, and easy removal using an external magnet, the $Cu_{0.5}Mg_{0.5}Fe_2O_4$–TiO_2 hybrid material can be employed as an effective photocatalyst for environmental remediation and treatment strategies. Further study on the photocatalytic performance of the $Cu_{0.5}Mg_{0.5}Fe_2O_4$–TiO_2 hybrid material for the photodegradation of other organic dyes as well as real dye-containing wastewater is essential.

CRediT authorship contribution statement

Chinh Van Tran: Investigation, Writing – original draft, Methodology, Formal analysis, Data curation. **Duong Duc La:** Investigation, Writing – original draft, Methodology, formal analysis, Data curation. **Phuong Nguyen Thi Hoai:** Methodology, Formal analysis, Resources. **H. Duc Ninh:** Methodology, Formal analysis, Resources. **T.H. Phuong Nguyen:** Methodology, Data curation, Review. **Thu Ha T. Vu:** Methodology, Data curation, Review. **Ashok Kumar Nadda:** Methodology, Resources, Review. **X. Cuong Nguyen:** Methodology, Resources, Review. **D. Duc Nguyen:** Supervision, Investigation, Project administration, Conceptualization, Writing – review & editing. **Huu Hao Ngo:** Supervision, Investigation, Conceptualization, Writing – review &
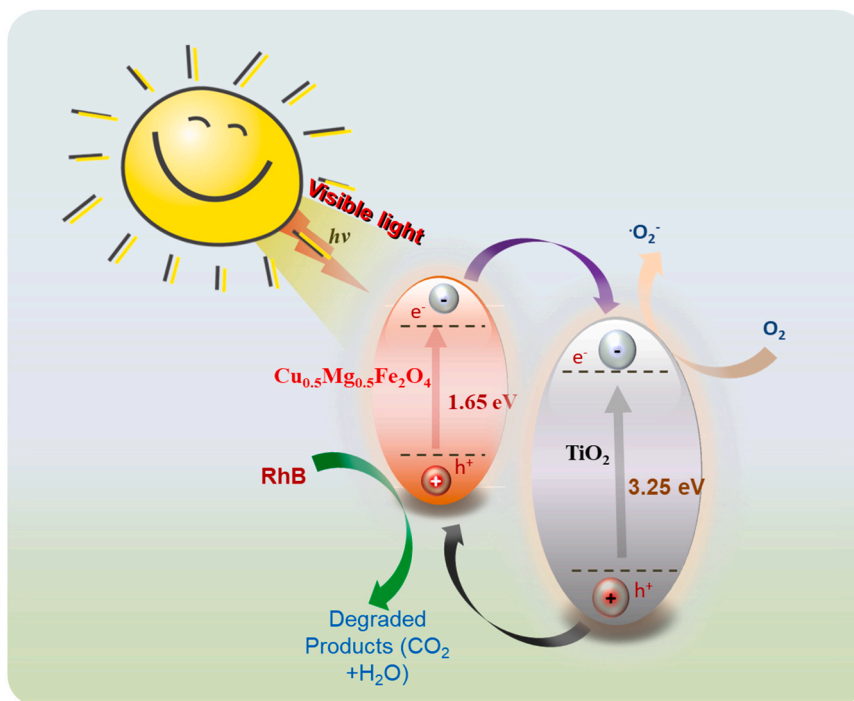
Fig. 10. Plausible mechanism concerning photocatalytic activity of $Cu_{0.5}Mg_{0.5}Fe_2O_4$–TiO_2 hybrid materials for RhB degradation under simulated sunlight irradiation.

editing.

References

Ahmed, M., Afify, H., El Zawawia, I., Azab, A., 2012. Novel structural and magnetic properties of Mg doped copper nanoferrites prepared by conventional and wet methods. J. Magn. Magn. Mater. 324, 2199–2204.

Almessiere, M., Korkmaz, A.D., Slimani, Y., Nawaz, M., Ali, S., Baykal, A., 2019. Magneto-optical properties of rare earth metals substituted Co-Zn spinel nanoferrites. Ceram. Int. 45, 3449–3458.

Almessiere, M.A., Slimani, Y., Baykal, A., 2020. Synthesis and characterization of Co1–2xNixMnxCeyFe2–yO4 nanoparticles. J. Rare Earths 38, 188–194.

Arifin, M.N., Karim, K.M.R., Abdullah, H., Khan, M.R., 2019a. Synthesis of titania copper ferrite photocatalyst and its photoactivity towards methylene blue degradation under visible light irradiation. Bull. Chem. React. Eng. Catal. 14, 219–227.

Asadi, R., Abdollahi, H., Gharabaghi, M., Boroumand, Z., 2020. Effective removal of Zn (II) ions from aqueous solution by the magnetic MnFe2O4 and CoFe2O4 spinel ferrite nanoparticles with focuses on synthesis, characterization, adsorption, and desorption. Adv. Powder Technol. 31, 1480–1489.

Baig, R.B.N., Varma, R.S., 2013. Magnetically retrievable catalysts for organic synthesis. Chem. Commun. 49, 752–770.

S.V. Bhosale, D.D. La, 2018. Nanoscale porphyrin superstructures: properties, self-assembly and photocatalytic applications. In: Nanoscience. pp. 57–85.

Bulut, E., Özacar, M., Şengil, İ.A., 2008. Equilibrium and kinetic data and process design for adsorption of Congo Red onto bentonite. J. Hazard. Mater. 154, 613–622.

Chen, Z., Wang, T., Jin, X., Chen, Z., Megharaj, M., Naidu, R., 2013. Multifunctional kaolinite-supported nanoscale zero-valent iron used for the adsorption and degradation of crystal violet in aqueous solution. J. Colloid Interface Sci. 398, 59–66.

Cho, S., Jung, S.-H., Lee, K.-H., 2008. Morphology-controlled growth of ZnO nanostructures using microwave irradiation: from basic to complex structures. J. Phys. Chem. C 112, 12769–12776.

Ciocarlan, R.-G., Seftel, E.M., Mertens, M., Pui, A., Mazaj, M., Tusar, N.N., Cool, P., 2018. Novel magnetic nanocomposites containing quaternary ferrites systems Co0. 5Zn0. 25M0. 25Fe2O4 (M= Ni, Cu, Mn, Mg) and TiO2-anatase phase as photocatalysts for wastewater remediation under solar light irradiation. Mater. Sci. Eng. B 230, 1–7.

Debnath, S., Das, R., 2020. Study of the optical properties of Zn doped Mn spinel ferrite nanocrystals shows multiple emission peaks in the visible range–a promising soft ferrite nanomaterial for deep blue LED. J. Mol. Struct. 1199, 127044.

Dom, R., Subasri, R., Radha, K., Borse, P.H., 2011. Synthesis of solar active nanocrystalline ferrite, MFe2O4 (M: Ca, Zn, Mg) photocatalyst by microwave irradiation. Solid State Commun. 151, 470–473.

Du, J., Bao, J., Fu, X., Lu, C., Kim, S.H., 2016. Facile preparation of S/Fe composites as an effective peroxydisulfate activator for RhB degradation. Sep. Purif. Technol. 163, 145–152.

Elayakumar, K., Manikandan, A., Dinesh, A., Thanrasu, K., Raja, K.K., Kumar, R.T., Slimani, Y., Jaganathan, S., Baykal, A., 2019. Enhanced magnetic property and antibacterial biomedical activity of Ce3+ doped CuFe2O4 spinel nanoparticles synthesized by sol-gel method. J. Magn. Magn. Mater. 478, 140–147.

Golshan, M., Kakavandi, B., Ahmadi, M., Azizi, M., 2018. Photocatalytic activation of peroxymonosulfate by TiO2 anchored on cupper ferrite (TiO2@ CuFe2O4) into 2, 4- D degradation: process feasibility, mechanism and pathway. J. Hazard. Mater. 359, 325–337.

Hafeez, H.Y., Lakhera, S.K., Karthik, P., Anpo, M., Neppolian, B., 2018. Facile construction of ternary CuFe2O4-TiO2 nanocomposite supported reduced graphene oxide (rGO) photocatalysts for the efficient hydrogen production. Appl. Surf. Sci. 449, 772–779.

Hannachi, E., Slimani, Y., Salem, M.B., Hamrita, A., Mani, D., Salem, M.B., Azzouz, F.B., 2015. Magneto-conductivity fluctuation in YBCO prepared by sintering of ball-milled precursor powder. Mater. Chem. Phys. 159, 185–193.

Jacob, B.P., Kumar, A., Pant, R., Singh, S., Mohammed, E., 2011. Influence of preparation method on structural and magnetic properties of nickel ferrite nanoparticles. Bull. Mater. Sci. 34, 1345–1350.

Jadhav, R.W., La, D.D., Truong, T.N., Khalap, S.V., Quang, D.V., Bhosale, S.V., 2020. The controllable nanostructure and photocatalytic behaviour of 5, 10, 15, 20-tetra-(3, 4, 5 trimethoxyphenyl) porphyrin through solvophobic supramolecular self-assembly. New J. Chem. 44, 18442–18448.

Kang, D., Yu, X., Ge, M., Song, W., 2015. One-step fabrication and characterization of hierarchical MgFe2O4 microspheres and their application for lead removal. Microporous Mesoporous Mater. 207, 170–178.

Kumar, S.S., Kumar, V., Malyan, S.K., Sharma, J., Mathimani, T., Maskarenj, M.S., Ghosh, P.C., Pugazhendhi, A., 2019. Microbial fuel cells (MFCs) for bioelectrochemical treatment of different wastewater streams. Fuel 254, 115526. La,

D.D., Tran, C.V., Hoang, N.T., Ngoc, M.D.D., Nguyen, T.P., Vo, H.T., Ho, P.H., Nguyen, T.A., Bhosale, S.V., Nguyen, X.C., 2020. Efficient photocatalysis of organic dyes under simulated sunlight irradiation by a novel magnetic CuFe2O4@ porphyrin nanofiber hybrid material fabricated via self-assembly. Fuel 281, 118655. Z., Chen, C., Wang, X., 2014. Hierarchical GOs/Fe 3 O 4/PANI magnetic

Li, J., Song, Z., Chen, C., Wang, X., 2014. Hierarchical GOs/Fe 3 O 4/PANI magnetic composites as adsorbent for ionic dye pollution treatment. RSC Adv. 4, 38192–38198.

Li, Q., Guo, B., Yu, J., Ran, J., Zhang, B., Yan, H., Gong, J.R., 2011. Highly efficient visible-light-driven photocatalytic hydrogen production of CdS-cluster-decorated graphene nanosheets. J. Am. Chem. Soc. 133, 10878–10884.

Li, Z.-J., Wang, L., Yuan, L.-Y., Xiao, C.-L., Mei, L., Zheng, L.-R., Zhang, J., Yang, J.-H., Zhao, Y.-L., Zhu, Z.-T., 2015. Efficient removal of uranium from aqueous solution by zero-valent iron nanoparticle and its graphene composite. J. Hazard. Mater. 290, 26–33.

Liu, T., Wang, L., Lu, X., Fan, J., Cai, X., Gao, B., Miao, R., Wang, J., Lv, Y., 2017. Comparative study of the photocatalytic performance for the degradation of different dyes by ZnIn 2 S 4: adsorption, active species, and pathways. RSC Adv. 7, 12292–12300.

J. Manzoor, M. Sharma, 2020. Impact of textile dyes on human health and environment. In: Impact of Textile Dyes on Public Health and the Environment, IGI Global. pp. 162–169.

Merouani, S., Hamdaoui, O., Saoudi, F., Chiha, M., Pétrier, C., 2010. Influence of bicarbonate and carbonate ions on sonochemical degradation of Rhodamine B in aqueous phase. J. Hazard. Mater. 175, 593–599.

Mohit, K., Gupta, V.R., Gupta, N., Rout, S., 2014. Structural and microwave characterization of Ni0. 2CoxZn0. 8− xFe2O4 for antenna applications. Ceram. Int. 40, 1575–1586.

Mostafa Hosseini Asl, S., Ghadi, A., Sharifzadeh Baei, M., Javadian, H., Maghsudi, M., Kazemian, H., 2018. Porous catalysts fabricated from coal fly ash as cost-effective alternatives for industrial applications: a review. Fuel 217, 320–342.

Nakhate, A.V., Yadav, G.D., 2017. Hydrothermal synthesis of CuFe2O4 magnetic nanoparticles as active and robust catalyst for N-arylation of indole and imidazole with aryl halide. ChemistrySelect 2, 2395–2405.

Nasir Baig, R.B., Nadagouda, M.N., Varma, R.S., 2015. Magnetically retrievable catalysts for asymmetric synthesis. Coord. Chem. Rev. 287, 137–156.

Natarajan, T.S., Natarajan, K., Bajaj, H.C., Tayade, R.J., 2013. Enhanced photocatalytic activity of bismuth-doped TiO 2 nanotubes under direct sunlight irradiation for degradation of Rhodamine B dye. J. Nanopart. Res. 15, 1–18.

Neris, A., Schreiner, W., Salvador, C., Silva, U.C., Chesman, C., Longo, E., Santos, I., 2018. Photocatalytic evaluation of the magnetic core@ shell system (Co, Mn) Fe2O4@ TiO2 obtained by the modified Pechini method. Mater. Sci. Eng. B 229, 218–226.

Piña-Pérez, Y., Tzompantzi-Morales, F., Pérez-Hernández, R., Arroyo-Murillo, R., Acevedo-Peña, P., Gómez-Romero, R., 2017. Photocatalytic activity of Al2O3 improved by the addition of Ce3+/Ce4+ synthesized by the sol-gel method. Photodegradation of phenolic compounds using UV light. Fuel 198, 11–21.

Qin, Q., Liu, Y., Li, X., Sun, T., Xu, Y., 2018. Enhanced heterogeneous Fenton-like degradation of methylene blue by reduced CuFe 2 O 4. RSC Adv. 8, 1071–1077. Reitz, C., Suchomski, C., Haetge, J., Leichtweiss, T., Jagličić, Z., Djerdj, I., Brezesinski, T., 2012. Soft-templating synthesis of mesoporous magnetic CuFe 2 O 4 thin films with ordered 3D honeycomb structure and partially inverted nanocrystalline spinel domains. Chem. Commun. 48, 4471–4473.

Ren, G., Yang, L., Zhang, Z., Zhong, B., Yang, X., Wang, X., 2017. A new green synthesis of porous magnetite nanoparticles from waste ferrous sulfate by solid-phase reduction reaction. J. Alloy. Compd. 710, 875–879.

Robinson, T., McMullan, G., Marchant, R., Nigam, P., 2001. Remediation of dyes in textile effluent: a critical review on current treatment technologies with a proposed alternative. Bioresour. Technol. 77, 247–255.

Roy, P., Bera, J., 2006. Effect of Mg substitution on electromagnetic properties of (Ni0. 25Cu0. 20Zn0. 55) Fe2O4 ferrite prepared by auto combustion method. J. Magn. Magn. Mater. 298, 38–42.

Salleh, M.A.M., Mahmoud, D.K., Karim, W.A.W.A., Idris, A., 2011. Cationic and anionic dye adsorption by agricultural solid wastes: a comprehensive review. Desalination 280, 1–13.

Sandoval, A., Hernández-Ventura, C., Klimova, T.E., 2017. Titanate nanotubes for removal of methylene blue dye by combined adsorption and photocatalysis. Fuel 198, 22–30.

Seffati, K., Honarvar, B., Esmaeili, H., Esfandiari, N., 2019. Enhanced biodiesel production from chicken fat using CaO/CuFe2O4 nanocatalyst and its combination with diesel to improve fuel properties. Fuel 235, 1238–1244.

Shen, Y., Wu, Y., Li, X., Zhao, Q., Hou, Y., 2013. One-pot synthesis of MgFe2O4 nanospheres by solvothermal method. Mater. Lett. 96, 85–88.

Slimani, Y., Almessiere, M., Güner, S., Tashkandi, N., Baykal, A., Sarac, M., Nawaz, M., Ercan, I., 2019a. Calcination effect on the magneto-optical properties of vanadium substituted NiFe 2 O 4 nanoferrites. J. Mater. Sci. Mater. Electron. 30, 9143–9154.

Slimani, Y., Almessiere, M., Korkmaz, A.D., Guner, S., Güngüneş, H., Sertkol, M., Manikandan, A., Yildiz, A., Akhtar, S., Shirsath, S.E., 2019b. Ni0. 4Cu0. 2Zn0. 4TbxFe2-xO4 nanospinel ferrites: ultrasonic synthesis and physical properties. Ultrason. Sonochem. 59, 104757.

Slimani, Y., Almessiere, M., Nawaz, M., Baykal, A., Akhtar, S., Ercan, I., Belenli, I., 2019c. Effect of bimetallic (Ca, Mg) substitution on magneto-optical properties of NiFe2O4 nanoparticles. Ceram. Int. 45, 6021–6029.

Šutka, A., Käämbre, T., Pärna, R., Döbelin, N., Vanags, M., Smits, K., Kisand, V., 2016. Ag sensitized TiO 2 and NiFe 2 O 4 three-component nanoheterostructures: synthesis, electronic structure and strongly enhanced visible light photocatalytic activity. RSC Adv. 6, 18834–18842.

Tran, C.V., Quang, D.V., Nguyen Thi, H.P., Truong, T.N., La, D.D., 2020. Effective removal of Pb (II) from aqueous media by a new design of Cu–Mg binary ferrite. ACS Omega 5, 7298–7306.

Xu, C., Anusuyadevi, P.R., Aymonier, C., Luque, R., Marre, S., 2019. Nanostructured materials for photocatalysis. Chem. Soc. Rev. 48, 3868–3902.

Zaki, H., Al-Heniti, S., Elmosalami, T., 2015. Structural, magnetic and dielectric studies of copper substituted nano-crystalline spinel magnesium zinc ferrite. J. Alloy. Compd. 633, 104–114.

Zhang, G.-Y., Sun, Y.-Q., Gao, D.-Z., Xu, Y.-Y., 2010. Quasi-cube ZnFe2O4 nanocrystals: hydrothermal synthesis and photocatalytic activity with TiO2 (Degussa P25) as nanocomposite. Mater. Res. Bull. 45, 755–760.

Zhou, Y., Chen, W., Shen, Y., Wu, X., Wu, W., Wu, J., 2015. Lattice strains and magnetic properties evolution of copper–magnesium ferrite with lithium substitution. J. Magn. Magn. Mater. 396, 198–203.

Zhu, X., Yuan, W., Lang, M., Zhen, G., Zhang, X., Lu, X., 2019. Novel methods of sewage sludge utilization for photocatalytic degradation of tetracycline-containing wastewater. Fuel 252, 148–156.